THE ASTROPHYSICAL JOURNAL, 436:203–215, 1994 November 20

ULTRAVIOLET-ILLUMINATED MOLECULAR CLOUD BOUNDARIES: EXTENDED [C II] 158 MICRON EMISSION TOWARD L1630

D. T. JAFFE[1]
Department of Astronomy, R.L.M. 15.308, University of Texas, Austin, TX 78712
S. ZHOU
Department of Astronomy, University of Illinois, 1002 West Green Street, Urbana, IL 61801
J. E. HOWE[2]
Department of Astronomy, University of Maryland, College Park, MD 20742
F. HERRMANN, S. C. MADDEN,[3] A. POGLITSCH, AND P. P. VAN DER WERF[4]
Max-Planck-Institut für extraterrestrische Physik, Postfach 1603, 85740 Garching bei München, Germany
AND
G. J. STACEY
Department of Astronomy, Cornell University, 512 Space Sciences Building, Ithaca, NY 14853
Received 1993 December 27; accepted 1994 May 11

ABSTRACT

We have made a large-scale map of the 158 μm C^+ line toward the L1630/Orion B molecular cloud. The map covers a $\sim 35' \times 45'$ area which includes the NGC 2024 H II region, ζ Ori, the reflection nebula NGC 2023, and the Horsehead nebula. Emission in the [C II] line is very widespread. The line was detected at levels in excess of a few 10^{-4} ergs cm^{-2} s^{-1} sr^{-1} over almost the entire mapped region. Extended emission associated with the NGC 2024 H II region and its envelope accounts for more than half of the [C II] flux. Over this $\sim 1.5 \times 2.5$ pc region, the amount of gas-phase carbon in the form of C^+ is comparable to the amount of carbon in CO. This result, together with the [C II] distribution, implies that [C II] emission arises on the surfaces of clumps throughout the cloud rather than in a single layer at the H II region boundary. Away from the H II region, most of the [C II] emission comes from the western edge of the L1630 cloud and probably results from excitation by external OB stars. The overall extent of the [C II] emission is comparable to that of millimeter molecular lines, but the distributions are different in detail. The difference in [C II] and molecular line distributions, in particular, the larger extent of the [C II] emission west of NGC 2024 implies large variations in the ratio of the [C II] and CO $J = 1 \rightarrow 0$ intensities. Models of photon-dominated regions can explain the relation between [C II] and CO intensities only if one considers the cloud edges and cloud interior separately. We propose a method for using [C II] and radio continuum emission to characterize the relationship between OB stars and photon-dominated regions.

Subject headings: H II regions — infrared: ISM: continuum — ISM: individual (L1630) — ISM: molecules — ISM: structure

1. INTRODUCTION

This paper presents the first detailed (1′ resolution) look at the large-scale [C II] emission from a giant molecular cloud. The results tell us about the physics and structure of the regions where the [C II] emission arises. We can also use these results as a guide to the interpretation of larger scale measurements both of [C II] emission from the dense interstellar medium in the Galaxy and of large-scale [C II] emission from other galaxies.

A basic observational and theoretical framework for understanding the emission from the ground state of ionized carbon already exists. The 158 μm C^+ $^2P_{3/2} \rightarrow {}^2P_{1/2}$ transition is one of the major coolants of the dense, neutral interstellar medium. Alone, it accounts for around 0.3% of the total far-IR luminosity of late-type spiral galaxies (Stacey et al. 1991; Wright et al. 1991). Analyses of possible sources of the [C II] line point to dense, partially ionized regions on the surfaces of molecular clouds as the dominant emitters of this radiation (Stacey et al. 1985; Crawford et al. 1985). Both in our own and other galaxies, however, the ionized medium and neutral atomic clouds may also contribute to the global [C II] emission (Wright et al. 1991; Shibai et al. 1991; Madden et al. 1993). The [C II] radiation arises in the outer layers of the clouds where far-UV photons with 91 nm $< \lambda <$ 110 nm can dissociate CO and ionize neutral carbon. Photoejection of electrons from grains by the far-UV radiation as well as far-UV radiative excitation of H_2 followed by collisional de-excitation heat the gas sufficiently to populate the C^+ $^2P_{3/2}$ level (e.g., De Jong, Dalgarno, & Boland 1980; Tielens & Hollenbach 1985; van Dishoeck & Black 1988; Sternberg & Dalgarno 1989). As a result, emission in the [C II] line traces the locations where far-UV radiation strikes dense neutral gas and creates photodissociation or photon-dominated regions (PDRs).

A detailed, large-scale [C II] map of a molecular cloud complex can yield information about PDRs on both large and

[1] Also Max-Planck-Institut für extraterrestrische Physik.
[2] Current address: FCRAO, University of Massachusetts, Amherst, MA 01003.
[3] Current address: NASA/Ames Research Center, Moffett Field, CA 94035.
[4] Current address: Sterrewacht Leiden, P.O. Box 9513, 2300 RA Leiden, Netherlands.

small scales. It can therefore link our understanding of the relationship between local cloud conditions and [C II] emission with our knowledge of where the global cooling in atomic fine structure lines occurs within the mostly neutral gas. On the large scales, we want to know which stars are responsible for the global [C II] emission from galaxies and how the strength and distribution of the [C II] emission relates to the structure of atomic and molecular clouds. The O and B stars that dominate the production of far-UV radiation spend most of their main-sequence lifetimes outside of molecular clouds (Mezger 1978; Bash, Green, & Peters 1977). The amount of far-UV radiation required to partially ionize and heat a significant layer on the neutral material, however (see Hollenbach, Takahashi & Tielens 1991 for recent models), implies that only OB stars embedded within or relatively close to (within 5–10 pc of) dense neutral clouds can participate significantly in exciting the [C II] emission. Nevertheless, observations on large scales in our own Galaxy show that much of the [C II] emission comes from extended regions and not from the areas right around embedded protostellar cores (Stacey et al. 1985; Matsuhara et al. 1989; Shibai et al. 1991; Nakagawa et al. 1993). While some of this extended emission may result from far-UV illumination by external OB stars, there is evidence that UV radiation from embedded stars propagating through a low-density interclump medium accounts for much of the extended emission (Stutzki et al. 1988; Howe et al. 1991).

On smaller scales within clouds, we want to understand the relationship between the cloud structure, the location of UV sources, the propagation of far-UV radiation, and the distribution of [C II] emission. Even within the dense interstellar gas, we do not have a firm picture of where most of the [C II] emission comes from. Does it come from right around compact H II regions? From clump surfaces throughout clouds? From interclump gas? From the outer layers of clouds near external OB stars? Or does the [C II] arise on the overall cloud surface in regions where the far-UV field is somewhat enhanced over typical values? The detailed observations that this paper presents address this issue for a single molecular cloud complex. Our earlier attempts to address this question (Stutzki et al. 1988; Howe et al. 1991; Stacey et al. 1993) were hampered by an inability to measure large-scale emission accurately while at the same time retaining sensitivity to small-scale features in the [C II] distribution.

How well do the PDR models predict the strength and distribution of the [C II] line and its relation to the distribution of ^{12}CO $J = 1 \rightarrow 0$ emission? The general agreement of the [C II] observations with theoretical predictions testifies to the overall soundness of the models. To date, however, observational verification of the models has been limited mostly to regions in the high-density, high-UV flux regime where the [C II] emission depends only weakly on the physical conditions. Also, the comparisons have used heterogeneous samples where it is possible to ascribe differences between observed and predicted line strengths to real variations in quantities held constant in the models. By studying a large portion of a single cloud within which there are a variety of UV fields, densities, and geometries, we can test the models over a larger range of parameter space in a situation where other physical and observational variables such as metallicity and linear beam size are not important. Our previous work has made clear that topology plays a major role in the total [C II] luminosity of a cloud (Howe et al. 1991). Clumpy clouds have much higher total [C II] cooling than homogeneous clouds. Are there other connections between the cloud structure and the [C II] emission?

We have chosen the NGC 2024/Orion B cloud as the target for our study. This cloud is nearby ($d \simeq 415$ pc; Anthony-Twarog 1982) and therefore has a favorable linear scale for our [C II] observations ($1' = 0.12$ pc). There is little or no foreground or background emission since the cloud is at high galactic latitude. The absence of line of sight confusion is important since the [C II] measurements are not velocity resolved. The cloud contains a large variety of interesting features—an H II region (NGC 2024), a nearby external O star (ζ Ori), edge regions with more distant OB stars (e.g., the Horsehead nebula; Zhou et al. 1993), a B-star reflection nebula (NGC 2023; Jaffe et al. 1990; Howe et al. 1991), and large regions with only weak far-UV illumination. L1630 is well studied in molecular lines and has been surveyed for embedded stellar sources (Lada 1990).

2. OBSERVATIONS

We observed the 157.74 μm $^2P_{3/2} \rightarrow {}^2P_{1/2}$ line of C^+ toward the L1630/NGC 2024/Orion B cloud in 1990 and 1991 September. For these observations, we used the MPE/UCB Far-Infrared Imaging Fabry-Perot Interferometer (FIFI: Poglitsch et al. 1991) on the 0.9 m telescope of the NASA–Kuiper Airborne Observatory. FIFI has 25 stressed Ge:Ga detectors arranged in a 5×5 array (Stacey et al. 1992). The instrument optics result in beam sizes of 55″ FWHM ($\Omega = 8.3 \times 10^{-8}$ sr) with a 40″ spacing between adjacent beams. The detectors view the sky through a fourth-order Fabry-Perot filter used as an order sorter for a scanning Fabry-Perot. For the observations reported here, the scanning Fabry-Perot was operated in 120th order, resulting in a spectral resolution of 51 km s^{-1}. For all but one of the five flights on which we made the observations, a "K mirror" at the entrance to the system maintained a constant (north–south) orientation of the array on the sky and produced a regular grid of observations at 40″ intervals. During the observations, the typical system noise-equivalent power (NEP) of the individual detectors was $\sim 5 \times 10^{-15}$ W Hz$^{-1/2}$.

Ordinarily, airborne far-IR spectroscopy has been done by rapidly switching the telescope secondary mirror between two positions on the sky and synchronously demodulating the resulting difference signal to reduce the effects of fluctuations in the instrument and sky background. With a scanning monochromator like a Fabry-Perot, the wavelength of the high-resolution element is either held at the position of the line or swept slowly across a relevant spectral band. Airborne spectrometers employing chopping secondary mirrors usually perform with sensitivities close to the limit imposed by the thermal background. The KAO chopping secondary, however, limits the spacing between the object and the reference beam to less than 7–9′. This limit severely hampers the study of extended emission.

We made the observations of L1630 using a frequency-switching technique. The telescope secondary remained stationary on the optical axis. We accomplished the short-timescale background subtraction by switching the center wavelength of the Fabry-Perot filter at 5 Hz between the observing wavelength and a reference wavelength at the center of our intended spectrum. The reference wavelength remained fixed as the observing wavelength was shifted across the spectrum to obtain a line profile. The resulting difference spectrum is stable for periods of 10–15 minutes. We removed the shape of the instrumental spectral response by observing a portion of sky 30′ to 1° away from the source and subtracting this "sky" spectrum from the source spectrum.

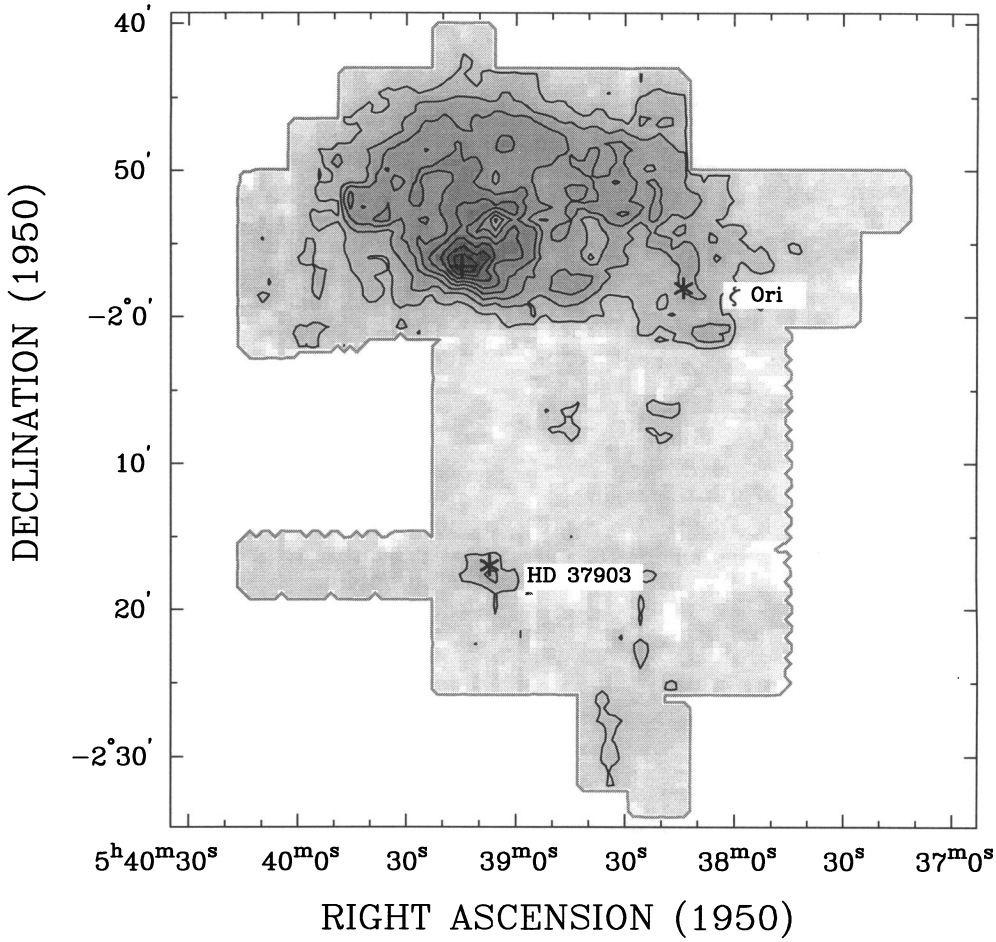

FIG. 1.—Distribution of the 158 μm [C II] emission toward the L1630/NGC 2024/Orion B cloud shown both as grayscale and contours. The lowest contour and contour interval are 3.6×10^{-4} ergs cm^{-2} s^{-1} sr^{-1}. The peak surface brightness is 3.1×10^{-3} ergs cm^{-2} s^{-1} sr^{-1} in an effective 60″ beam. The cross marks the position of the NGC 2024 IRS 1 and the peak of the NGC 2024 H II region (α[1950] = 05^{h}39^{m}14^s, δ[1950] = −01°57′00″). The northern star indicates the location of ζ Ori, an O9 supergiant. The southern star marks the position of HD 37903, the B1.5 star that excites the reflection nebula NGC 2023. The wavy line outlines the mapped region.

For most observations, we began by taking several frequency-switched spectral scans at the off-source reference position. We then made several (typically two to four) scans at each of three to four on-source positions spaced by 200″ in R.A. or decl., resulting in a complete source map at 40″ spacings. We repeated the off-source scans after each set of on-source measurements. About once an hour, we observed an internal, constant temperature load. The position solutions for these observations were accurate to better than 15″. About half of the mapped area was observed more than once with consistent results obtained from the multiple observations.

To obtain [C II] line fluxes, we first subtracted sky scans from source scans. Dividing this difference by observations of the constant temperature blackbody load corrected for channel-to-channel gain variations. A correction for the coupling of the instrument to the telescope was obtained by observations of Mars and of the continuum emission from Orion A. After fitting linear baselines to the observed spectra, we corrected for leakage, atmospheric transmission, and the presence of Lorentzian wings of the Fabry-Perot filter response in the parts of the spectrum used to fit the baseline. The peak intensity in our 55″ beam was 3.75×10^{-3} ergs cm^{-2} s^{-1} sr^{-1}. The absolute calibration is good to better than $\pm 30\%$. Relative calibration errors are 3–6 times smaller.

We observed the $J = 2 \rightarrow 1$ transitions of ^{12}CO, ^{13}CO, and C^{18}O in 1992 December with the Caltech Submillimeter Observatory 10.4 m telescope on Mauna Kea.[4] The beam size was 30″–34″ for all three lines. The coupling efficiency to sources from a few arcminutes in diameter (i.e., somewhat larger than the main beam) to the size of the moon was $80\% \pm 10\%$. We therefore divided the T_A^* values derived at the telescope by 0.8 to obtain a main beam temperature, T_{MB}.

3. RESULTS

Figure 1 shows the [C II] map of L1630. The map includes most of a 35′ by 45′ region centered between NGC 2023 and NGC 2024. We produced the map by regridding all of the data onto a common grid using a conical interpolation scheme with a 45″ interpolation radius. The effective beam size for the map in Figure 1 is therefore ∼60″. The peak [C II] intensity in the map in Figure 1 is 3.1×10^{-3} ergs cm^{-2} s^{-1} sr^{-1}. In 1990 September, we also observed the central part of NGC 2024 using a conventional chopping and beam-switching technique.

[4] The Caltech Submillimeter Observatory is operated by the California Institute of Technology under funding from National Science Foundation contract 90-15755.

The chopper throw for these measurements was ~7′ east–west. The measured peak surface brightness was ~20% lower than the frequency-switched value. This lower flux is in good agreement with the peak flux one would expect, given the amount of [C II] emission in the reference beams east and west of the source (see Fig. 1). Earlier measurements toward the peak of NGC 2024 with a 4′ × 7′ beam and an 11′ chopper throw (Kurtz et al. 1983) determined a peak surface brightness of 1.7×10^{-3} ergs cm^{-2} s^{-1} sr^{-1}. Smoothing our own data to the same resolution, and subtracting an estimate for emission in the reference beams of Kurtz et al. from the smoothed data, we obtain a value of 1.4×10^{-3} ergs cm^{-2} s^{-1} sr^{-1}. The four panels in Figure 2 compare a smoothed (1.′8 resolution) version of the [C II] map to maps of CO and ^{13}CO $J = 1 \rightarrow 0$ and CS $J = 2 \rightarrow 1$ over the same field with similar resolution (Lada, Bally, & Stark 1991; Peterson & Bally 1994). Figure 3 shows a comparison of the 60″ resolution [C II] distribution to the distribution of ^{12}CO, ^{13}CO, and C^{18}O $J = 2 \rightarrow 1$ intensity measured along an east–west cut through the peak of NGC 2024 with the CSO at ~30″ resolution. The total [C II] flux arising in the mapped region is 4.4×10^{-8} ergs cm^{-2} s^{-1}. At a distance of 415 pc, this corresponds to a [C II] luminosity of 230 $L_{\odot}$.

3.1. *The NGC 2024 Complex*

The mapped region divides morphologically into a large, bright northern complex associated with NGC 2024 (north of $\delta = -02°03'$), a weaker and more diffuse emission region in the southern area surrounding NGC 2023, and an emission region along the western edge of the cloud (west of $\alpha = 05^h38^m34^s$; see also Zhou et al. 1993). The northern complex accounts for more than half of the [C II] emission from the mapped region. In this complex, the [C II] distribution has a sharp central peak close to the position of the peak of NGC 2024. The region above the 70% contour level is only 2.′5 (0.3 pc) in diameter. The region above the 50% contour is 6′ × 7′. Most of the emission, however, arises from an extended plateau surrounding this central peak. At the 20% level, this plateau extends 24′ (2.9 pc) east–west and 14′ (1.7 pc) north–south. The outer edges of the plateau are well-defined and rather sharp. Except in the west, near ζ Ori, the [C II] brightness drops from 30% to 10% of the peak value in 0.3 pc or less.

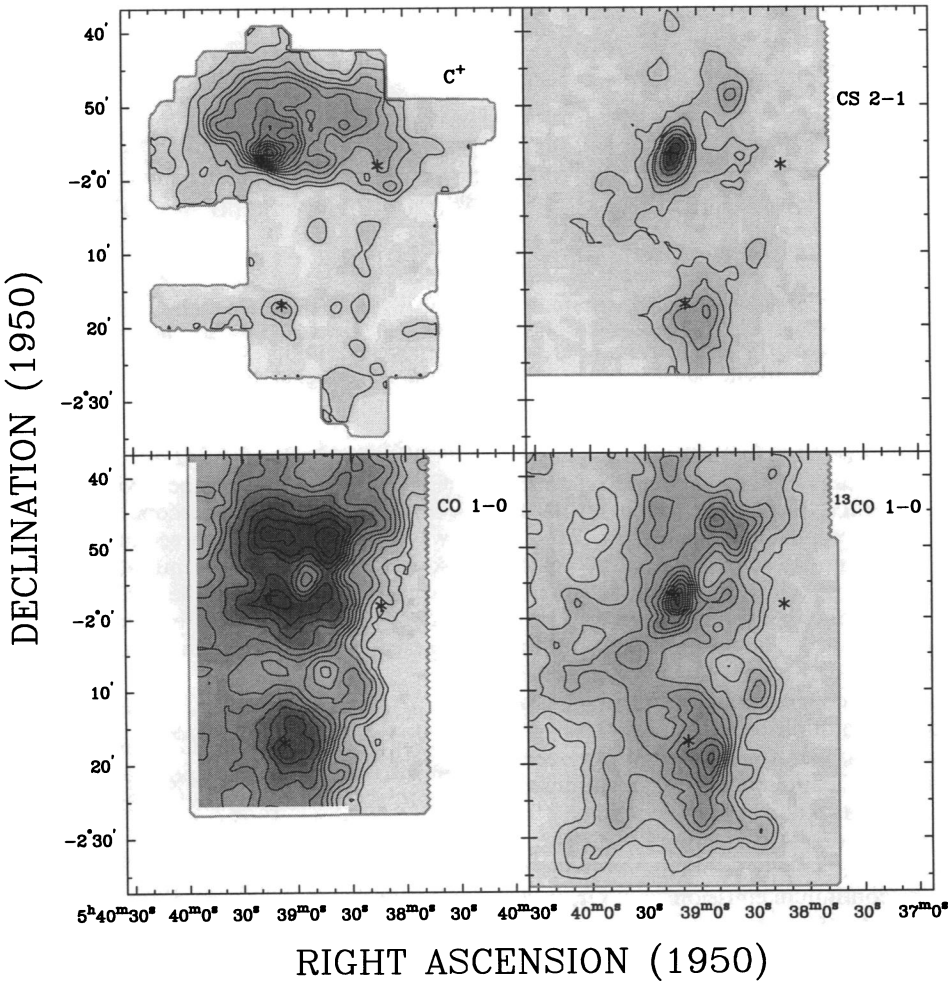

FIG. 2.—Comparison of [C II] and molecular line emission toward L1630. All maps have been smoothed to an effective resolution of 1.′8–2.′0 and are displayed as contours superposed on grayscale. The wavy lines outline the mapped regions. The cross and stars are as in Fig. 1. *Upper left*: the [C II] 158 μm distribution. The lowest contour and contour interval are 1.85×10^{-4} ergs cm^{-2} s^{-1} sr^{-1}. *Upper right*: Integrated line strength for CS $J = 2 \rightarrow 1$ (Lada et al. 1991). The contour levels are 1, 2, 3, 4, 7, 10, and 13 K km s^{-1}. *Lower left*: ^{12}CO $J = 1 \rightarrow 0$ integrated line strength (Peterson & Bally 1993). The lowest contour and contour interval are 10 K km s^{-1}. *Lower right*: ^{13}CO $J = 1 \rightarrow 0$ integrated line strength (Peterson & Bally 1994). The lowest contour and contour interval are 5 K km s^{-1}.

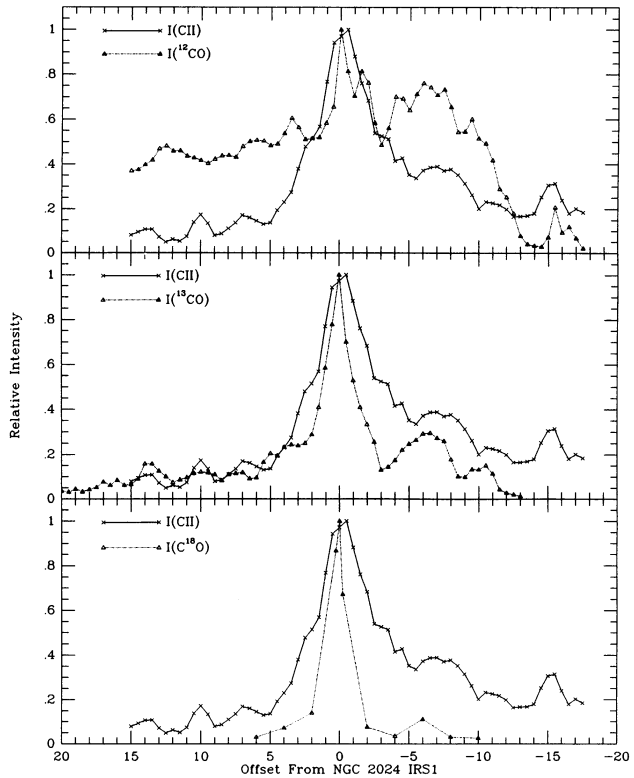

FIG. 3.—Cross scans along $\delta(1950) = -01°57'00''$. The effective resolution along the [C II] scan is 60″. The molecular line data were taken at the points shown with a ~32″ beam. The peak values along the scans are: $I([C\ II]) = 2.8 \times 10^{-3}$ ergs cm^{-2} s^{-1} sr^{-1}, $I(^{12}CO\ J = 2 \rightarrow 1) = 202$ K km s^{-1}, $I(^{13}CO\ J = 2 \rightarrow 1) = 85.8$ K km s^{-1}, and $I(C^{18}O\ J = 2 \rightarrow 1) = 18.4$ K km s^{-1}.

The drop is especially steep south of NGC 2024 where the drop from the peak to the 10% contour occurs in a space of only 3′. The northern complex exhibits a good deal of structure. The hole in the [C II] distribution to the north of the peak and the north–south ridge near ζ Ori appear independently in both the 1990 and 1991 datasets.

3.2. *The Southern Cloud and NGC 2023*

South of NGC 2024, the [C II] emission is almost everywhere less than 15% of the peak surface brightness. For one 200″ square 10′ due south of NGC 2024, a longer integration resulted in a detection of [C II] emission at a level of 2.5×10^{-4} ergs cm^{-2} s^{-1} sr^{-1}, or ~7% of the peak surface brightness. Much of the remaining area in the southern part of the map has [C II] emission at a comparable level. The brightest region is only 9×10^{-4} ergs cm^{-2} s^{-1} sr^{-1} (~25% of the peak of NGC 2024). This secondary maximum lies toward NGC 2023, about 30″ from the peak position in our earlier [C II] map (Jaffe et al. 1990; Howe et al. 1991). The peak surface brightness is within 10% of the Howe et al. value.

3.3. *The Western Edge*

Along the western edge of the cloud (~15′ west of the peak of NGC 2024 in the northern complex and ~10′ west of the NGC 2024 peak in the southern region), there is a ridge of enhanced [C II] emission. In the north, this emission roughly coincides with the right ascension of ζ Ori. Here the emission is 6–9 $\times 10^{-4}$ ergs cm^{-2} s^{-1} sr^{-1} and extends over a ~5′ × 15′ region. In the area 10′–30′ south of NGC 2024, some of the strongest [C II] emission comes from near the western cloud edge. A [C II] ridge is clearly visible north of −02°10′ and also in the southern part of the source. South of −02°26′, where the data are of extremely good quality, the [C II] ridge coincides to within the pointing errors (~ ±15″) with the cloud boundary seen in optical photographs (see Zhou et al. 1993). The [C II] emission along the part of the ridge from −02°26′ to −02°32′ is essentially unresolved in the east–west direction (thickness ≤0.′6). There is a ~3′ long east–west protrusion extending from the ridge at the declination of the optical Horsehead nebula (Zhou et al. 1993).

3.4. *Comparison with Other Emission*

The 1.4 GHz radio continuum emission toward NGC 2024 (van der Werf et al. 1993) has a distribution remarkably similar to that of the upper contours of the [C II] map. The peak positions and the morphology both agree well. The lower level [C II] emission, however, is much more extended than the 1.4 GHz continuum emission from the H II region. The 1.4 GHz emission has a total east–west extent of 10′ at 1% of the peak surface brightness in a 40″ beam, as compared to the 24′ east–west extent of the [C II] at the 20% level. The 15 GHz single dish observations of Krügel et al. (1982) agree with the source size derived at 1.4 GHz.

The [C II] emission in L1630 shares several morphological features with the emission in the ^{12}CO and ^{13}CO $J = 1 \rightarrow 0$, and CS $J = 2 \rightarrow 1$ transitions. The [C II] emission is more centrally peaked than the ^{12}CO emission but not as peaked as either the ^{13}CO or CS emission. The ^{13}CO and CS emission immediately south of the [C II] peak in NGC 2024 (cross in Fig. 2) extends south of the sharp boundary in the [C II] emission. In this part of the cloud, the dense, high column density molecular ridge that runs north–south behind the H II region dominates the ^{13}CO and CS emission (Mezger et al. 1988; Moore et al. 1989; Schulz et al. 1991; Graf et al. 1992). The ^{12}CO emission along the southern border of NGC 2024 extends slightly farther to the south than the [C II] emission. At the northern edge of NGC 2024, the [C II] and ^{12}CO emission cut off rather sharply at the same declination. The ^{13}CO emission shows a ridge with an intensity of 10 K km s^{-1}, 20% of the peak brightness, that continues through this sharp boundary.

In general, while the ^{12}CO emission provides the best match to the extent and the large-scale morphology of the [C II] emission, the ^{13}CO and the CS emission actually mirror more closely many of the details seen in [C II] at 1.′8 resolution. In NGC 2024, not only are the ^{13}CO, CS, and [C II] peaks coincident, but secondary maxima in the molecular maps to the northwest, west, and southeast of the peak coincide with fairly well-defined ridges in the [C II] distribution. In the southern part of the map, the [C II] emission edge coincides with the edge of the brightest peak in ^{13}CO and CS. To the north of this peak, a secondary maximum in the molecular emission coincides with a [C II] peak along the edge of the cloud.

The somewhat higher angular resolution east–west cut through the center of NGC 2024 (Fig. 3) offers a more detailed comparison of the [C II] and CO line distributions. The R.A. extents of the central peaks in [C II] and ^{12}CO $2 \rightarrow 1$ are very similar (Fig. 3, *top panel*). Outside the central 5′, both lines show broad emission plateaus. West of NGC 2024, the ^{12}CO $2 \rightarrow 1$ intensity drops very rapidly from ~100 K km s^{-1} to less than 10 K km s^{-1} (from ~50% to <10% of its peak value) as

one goes from 10′ to 13′ west of the central position. Over the same interval, the [C II] emission is fairly constant at a level of $\sim 6 \times 10^{-4}$ ergs cm^{-2} s^{-1} sr^{-1}. In the east, the ^{12}CO emission continues at ~ 90 K km s^{-1} from 5′ to at least 15′ from the NGC 2024 peak while the [C II] intensity drops slowly from 4×10^{-4} ergs cm^{-2} s^{-1} sr^{-1} to $\sim 3 \times 10^{-4}$ ergs cm^{-2} s^{-1} sr^{-1}.

One interesting detail shown in the ^{12}CO east–west cut is the drop in intensity near ζ Ori (the star lies 15′ west of the NGC 2024 peak, 1′ south of the cut. A small-scale map of the ζ Ori region in ^{12}CO $3 \rightarrow 2$ (Jaffe & Phillips 1992, unpublished) shows that the gap in the ^{12}CO emission along the cut between 13′ and 15′ west of NGC 2024 extends $\pm 2'$ north–south.

Over the inner 5′ of the cut shown in Figure 3, the bright molecular ridge behind the PDR causes a sharp difference in the ^{13}CO $2 \rightarrow 1$ and [C II] distributions (Fig. 3 *middle panel*). Beyond $\pm 4'$ the correspondence between the distributions is remarkably detailed. Each of the five subsidiary ^{13}CO peaks has a counterpart (within $\sim 1'$) in [C II]. The amount of peak-to-valley contrast (typically a factor of 1.5) is quite similar for the two species. Our C^{18}O cut agrees well with the ^{13}CO distribution except that the C^{18}O intensity away from the central peak is lower (Fig. 3, *lower panel*), as one might expect given the huge column densities toward the ridge (see Graf et al. 1993).

Thronson et al. (1984) mapped the central region of NGC 2024 in the continuum at 40, 60, 100, and 160 μm at $\leq 50''$ resolution. At 60 μm, the source is $\sim 4'$ east–west by $\sim 2'$ north–south at the 20% level. As with the radio continuum, there exists a good correspondence between the far-IR continuum distribution and the [C II] distribution, especially where the emission dies away quickly south of the peak. At longer submillimeter wavelengths, the cooler, high column density north–south ridge dominates the continuum emission (Mezger et al. 1988). The integrated far-IR emission in the Thronson et al. maps corresponds to $L = 2.8 \times 10^4\ L_\odot$ at a distance of 415 pc. The 60 μm and 100 μm maps from the *IRAS* Infrared Sky Survey Atlas indicate that there is about twice as much continuum emission from NGC 2024 as the less extensive maps of Thronson et al. account for. The total far-IR luminosity of the northern region is $\sim 5 \times 10^4\ L_\odot$. The global [C II] luminosity within the mapped region is therefore 0.4% of the far-IR luminosity.

4. DISCUSSION

4.1. *Local and Global Sources of* [C II] *Excitation*

4.1.1. *The NGC 2024 Plateau:* [C II] *from an* H II *Region Boundary*

Most of the [C II] emission from NGC 2024 arises in the predominantly neutral boundary layer of the molecular cloud where far-UV photons from the exciting stars of the H II region can strike the neutral gas. Except in the central few arcminute north–south strip, where there is an obscuring dust lane, the H II region clearly lies along the surface of the molecular cloud toward the Earth. We use the observed 1.4 and 15 GHz radio continuum flux from the nebula (van der Werf et al. 1993; Krügel et al. 1982) to derive a total number of Lyman continuum photons of $10^{47.9}$ s^{-1} (Rubin 1968), given a distance of 415 pc (Anthony-Twarog 1982). This corresponds to the emission one would expect from a single ZAMS O9.5 star (Panagia 1973). The far-IR luminosity implies a single-star spectral type of O9. For late O stars, much of the gas-phase carbon in the H II region is singly ionized. This material can emit in the 158 μm [C II] line. For dense H II regions, the ground-state levels of C^+ are populated according to their statistical weights and the strength of the 158 μm line depends only on the column density of C^+. Since NGC 2024 is a "blister" H II region on the front surface of a dense neutral cloud, its density must be substantially higher and its column density substantially lower than the column density one would estimate from the size of the radio continuum emission region and its emission measure (i.e., from the volume averaged density of the H II region, ~ 1300 cm^{-3}; Crutcher et al. 1986). It is therefore unlikely that the H II region contributes more than 10% to the observed peak [C II] brightness. Even if one uses the C^+ column density derived from the volume density, the H II region in NGC 2024 can be responsible for no more than 25% of peak [C II] brightness. Away from the radio peak, the contribution of the H II region to the observed [C II] is negligible (on average, the predicted [C II] intensity of the H II region is 3% of the observed intensity for an electron density of 10^3 cm^{-3}).

In order to evaluate the likelihood of [C II] emission from the photon-dominated neutral layer, we derived the far-UV flux (photons with energies between 6 and 13.6 eV) emerging from the ionizing source assuming that the star is a blackbody. This assumption gives UV flux estimates within $\sim 30\%$ of those based on LTE line-blanketed stellar models (Kurucz 1979). The radio continuum results imply that the far-UV luminosity is $2 \times 10^4\ L_\odot$ and that the unextincted far-UV flux is $G_0 = 2.7 \times 10^4$, in units of the mean value of the interstellar radiation field (1.6×10^{-3} ergs cm^{-2} s^{-1}), at a projected distance of 0.12 pc (1.′0) from the ionizing source. Why is the emission here near the [C II] peak, where the [C II] intensity is $\sim 3 \times 10^{-3}$ ergs cm^{-2} s^{-1} sr^{-1}, so much (a factor of 2–4) brighter than the general emission from the plateau? Two factors most likely share responsibility. The first of these is the high value of G_0 in the inner region. The PDR models predict [C II] intensities of $1\text{–}2 \times 10^{-3}$ ergs cm^{-2} s^{-1} sr^{-1} for gas densities of $10^4\text{–}10^5$ cm^{-3} and $G_0 = 2 \times 10^4$. A second possible effect is geometry. The [C II] peak lies to the south of the radio continuum peak in a region where kinematic evidence indicates that the dense material behind the H II region and the foreground dust lane join together (Crutcher et al. 1986; Barnes et al. 1989; Graf et al. 1993). This junction may result in significant foreshortening of the emission region, as seen from Earth. It may also shadow the southern part of the cloud as seen from the exciting stars and thereby cause the observed steep decline in [C II] intensity south of the peak. Two arcminutes from the center of NGC 2024, the UV field is no greater than the unextincted value, $G_0 = 5 \times 10^3$. For a field of this strength, the largest [C II] fluxes predicted by PDR models are $\sim 1 \times 10^{-3}$ ergs cm^{-2} s^{-1} sr^{-1} (van Dishoeck & Black 1988; Hollenbach et al. 1991; Stacey et al. 1991). This model [C II] flux is almost as large as the observed value.

A single far-UV source or group of sources near the radio continuum peak can account for the observed [C II] emission near the boundaries of the radio continuum source. Picture the radio continuum emission as arising from a flat or slightly bowl-shaped ionization front which lies approximately in the plane of the sky and has its ionizing source fairly close to the cloud surface near the continuum peak (e.g., Crutcher et al. 1986). If there is very little emission measure away from the ionization front and little absorption by dust, the radio continuum emission in outlying regions of the nebula should predict an incident far-UV flux identical with what one would expect from simple geometric dilution of the radiation arising near the

peak of the source. We perform this comparison for a region along the outer (0.1 Jy in a 1′ beam) contour of Krügel et al. (1982), about 6′ northeast of the peak. The radio continuum map implies a local far-UV intensity of $G_0 = 690$. Geometric dilution predicts a comparable value ($G_0 = 780$).

In our test region, 6′ northeast of the [C II] peak, photodissociation models predict [C II] brightnesses in the range 3–9 $\times 10^{-4}$ ergs cm^{-2} s^{-1} sr^{-1} for $G_0 = 750$ and densities between 5×10^3 and 2×10^5 cm^{-3}, if the far-UV photons are absorbed in the region immediately behind the radio continuum source (Wolfire, Hollenbach, & Tielens 1989; Stacey et al. 1991). This prediction is lower than or comparable to the observed value ($\sim 1.2 \times 10^{-3}$ ergs cm^{-2} s^{-1} sr^{-1}). Note however, that the assumption of a single ionizing source for NGC 2024 may result in an underestimate of G_0 by up to a factor of 2. For regions where G_0 is low, this can cause the models to underestimate the [C II] intensity.

Beyond 6′, the radio continuum emission is undetectable. If the far-UV flux continues to drop geometrically beyond the last radio contours, at the 10% [C II] contour (3.5×10^{-4} ergs cm^{-2} s^{-1} sr^{-1}), ~12′ northeast of the peak, G_0 should be around 165. The PDR models predict [C II] intensities of 1–5×10^{-4} ergs cm^{-2} s^{-1} sr^{-1} at this position, depending on the model and the density of the gas. The sharp drop in the [C II] brightness at the outer edge of the cloud occurs at the place where the calculated G_0 corresponds to the value for which the models predict that the [C II] intensities from high-density gas ($n >$ a few 10^3 cm^{-3}) should begin to fall rapidly as well. Greater than 10′ north of NGC 2024, where $G_0 \leq 200$, the various PDR models predict, for any gas density, [C II] line strengths which are 2–4 times lower than the observed strengths. Typical ^{13}CO column densities 5–10′ north and east of the center of NGC 2024 are a few 10^{16} cm^{-2}. For a ^{13}CO abundance of 2×10^{-6}, this implies a molecular hydrogen column density, $N_{H2} \simeq 10^{22}$. Given the ~3 pc linear size scale of the cloud, this implies an average density, $\langle n_{H2} \rangle = 10^3$ cm^{-3}. At the cloud surface, the density could be even lower. At a density of 10^3 cm^{-3}, the models predict [C II] intensities smaller than the observed intensities by a factor ~2–3. At lower densities, the difference between the model predictions and the observations would be even greater.

4.1.2. ζ Ori and the Western and Southern Cloud Edges

If ζ Ori lies somewhat in front of the L1630 cloud, its far-UV radiation can account for most of the diffuse [C II] flux from the western edge of the NGC 2024 cloud as well as from the entire region south of NGC 2024. The small hole in the ^{12}CO distribution near the position of ζ Ori (Fig. 3) might lead one to think that the star is close to the cloud (within 0.2–0.4 pc of the surface, given the size of the hole). It is surprising, therefore, that the CO lines (Figs. 2 and 3) and the far-IR continuum are so faint in the vicinity of the star. The local far-IR surface brightness detected by *IRAS* corresponds to a UV field G_0 ~300. For an O9.5I star, this implies that the star is ~5 pc in front of the cloud, unless most of the UV radiation is escaping out the back of the hole seen in the CO maps. A displacement from the cloud of 5 pc along the line of sight toward us does not affect the ability of ζ Ori to provide far-UV radiation sufficient to excite the [C II] in the Horsehead nebula (Zhou et al. 1993) or other regions along the southern ridge. Apart from NGC 2023 and the southern ridge, typical [C II] intensities over much of the region 15′–30′ south of NGC 2024 are $\sim 2 \times 10^{-4}$ ergs cm^{-2} s^{-1} sr^{-1}. If ζ Ori lies 5 pc in front of the cloud, the unextincted UV fluxes are ~170 times the mean interstellar radiation field in this region. Plane-parallel PDR models predict [C II] intensities of 2–8 $\times 10^{-4}$ ergs cm^{-2} s^{-1} sr^{-1} for this UV field, as long as the density is between 10^3 and 10^5 cm^{-3}. We have a more reliable measurement of the [C II] surface brightness for the region 10′ directly south of NGC 2024 (2.5×10^{-4} ergs cm^{-2} s^{-1} sr^{-1}). The unextincted UV flux from ζ Ori at this position ($G_0 \sim 200$) is sufficient to produce the observed [C II] surface brightness (van Dishoeck & Black 1988; Hollenbach et al. 1991; Stacey et al. 1991).

4.1.3. [C II] and Cloud Geometry

In earlier work (Stutzki et al. 1988; Howe et al. 1991; Stacey et al. 1993), we have invoked the existence of unresolved clumps with high density and a low volume filling factor to explain the extent and intensity of the [C II] emission from a variety of galactic clouds. The clumpy models help explain the data if the density of any interclump gas is low enough to permit UV photons to penetrate for long distances through the cloud. In L1630, most of the UV sources appear to lie at the surface or outside of the molecular cloud. As a result, direct UV illumination of the cloud boundary can explain the extent of the [C II] emission. Is it necessary for any other reason to invoke the clumpy structure needed elsewhere to explain the source morphology?

Geometric factors like orientation to the line of sight or the existence of clumps tend to raise the observed value of the [C II] intensity over the predictions made for plane-parallel slabs viewed perpendicular to their surface (see Zhou et al. 1993). In particular, a superposition of optically thin clump surfaces with unity area filling factor will have 4 times the brightness of a semi-infinite, plane-parallel layer filling the beam. In the above discussion, we have compared the observed intensities to PDR models under the assumption that both the observer and the source of far-UV radiation were normal to the surface of a single, plane-parallel, semi-infinite molecular cloud. The theory and observations agree relatively well since two of the most likely complications to the geometry—beam-filling factors less than unity and lower UV fluxes from oblique illumination of the cloud surfaces—tend to offset the other major effect, the increased [C II] emission from the larger surface area presented by a clumpy medium. The tight correlation between the ^{13}CO 2 → 1 and [C II] distributions (Fig. 3) presents perhaps the strongest argument for the association of the [C II] with the surfaces of individual clumps. A position-velocity diagram of the ^{13}CO $J = 2 \rightarrow 1$ cross scan in Figure 3 supports the clumpy picture of the NGC 2024 PDR. The diagram show a series of ~0.1–0.2 pc sized velocity-localized structures.

4.2. The Global Relationship between C^+ and CO

4.2.1. $I_{[C\,II]}$ vs. I_{CO} and Photodissociation Models

Crawford et al. (1985) first remarked on the extraordinary correlation between the intensity of the 158 μm C^+ line and the intensity of the $J = 1 \rightarrow 0$ transition of CO. As a number of people have pointed out, much of this correlation stems from the huge range in distances to the sources in the Crawford et al. sample and the resulting correlated variation in beam-filling factor (e.g., Wolfire et al. 1989). There are, however, reasons to expect a relationship between I(CO $J = 1 \rightarrow 0$) and I([C II]), even when the intensities are normalized to eliminate beam-filling factor effects. If both lines arise in the outer layers of UV illuminated molecular clouds, primarily in regions with dense

($n > 1000$ cm^{-3}) gas and large UV fields ($G_0 > 100$), the similar dependences on density and on UV intensity of the two lines should lead to a correlation of the two intensities, even when one removes the effects of filling factor (Wolfire et al. 1989; Stacey et al. 1991). The present L1630 sample is an ideal place to investigate the relationship between the [C II] and CO $J = 1 \rightarrow 0$ intensities. All of the data come from a source at a constant distance, there are a large number of points observed with the same equipment under similar conditions, and there are nevertheless a wide range of excitation conditions.

Figure 4 shows the relationship between the [C II] and ^{12}CO $J = 1 \rightarrow 0$ intensities for the region north of $-02°03'$. Overall, there is little apparent correlation between the intensities of the two lines. A more careful examination, however, reveals that the different parts of the source have very different distributions in the I([C II])–I(CO) plane. We have divided the source into two regions: the cloud proper (less than 10′ west of the radio peak, shown as solid dots in Fig. 4), and the western edge zone (10′ or farther west of the radio continuum peak, shown as open triangles). The points representing data taken toward the western edge zone stretch almost horizontally across the diagram with many points having very small CO $J = 1 \rightarrow 0$ intensities while still having [C II] intensities within a factor of 4 or so of the peak value. At least some of the points with the largest [C II]/CO $J = 1 \rightarrow 0$ intensity ratios lie along the true macroscopic edge of the cloud. For a cloud with a density of n(H) = 10^4 cm^{-3}, a column density of 3×10^{21} cm^{-2}, characteristic of the layer where the [C II] emission arises (Hollenbach et al. 1991), is reached 3×10^{17} cm into the cloud (a projected angle of 50″ at the distance of L1630). While some of the most extreme [C II]/CO intensity ratios may therefore be a result of having resolved the photodissociated layer at the edge of the cloud, many of the points with high [C II]/CO values lie 3′–4′ into the edge zone.

In both the cloud proper and western edge zone data sets, there is a significant I([C II])–I(CO) correlation. The slope of the relationship in the two regions, however, is radically different. A fit to the points within the cloud (east of $05^h38^m34^s$ and north of $-02°03'$) yields

$$\log (I([\text{C II}])) \simeq 9.7 + [1.9 \log (I(\text{CO}))] ,$$

while a fit to the points at the edge of the cloud (west of $05^h38^m34^s$ and north of $-02°03'$) yields

$$\log (I([\text{C II}])) \simeq -1.9 + [0.20 \log (I(\text{CO}))] .$$

In both cases, the dispersion about this relation is large. Interestingly, the two relations intersect at I([C II])/I(CO) = 3600 (where both intensities are expressed in the same units), close to the canonical ratio derived by Crawford et al. (1985).

The physical basis for the correlation between CO and [C II] intensity lies at least partly in the similar critical densities of the C^+ $^2P_{3/2} \rightarrow {}^2P_{1/2}$ and CO $J = 1 \rightarrow 0$ transitions. The solid lines in Figure 4 show the PDR models of Wolfire et al. (1989) superposed on our data. Most of the points from the cloud

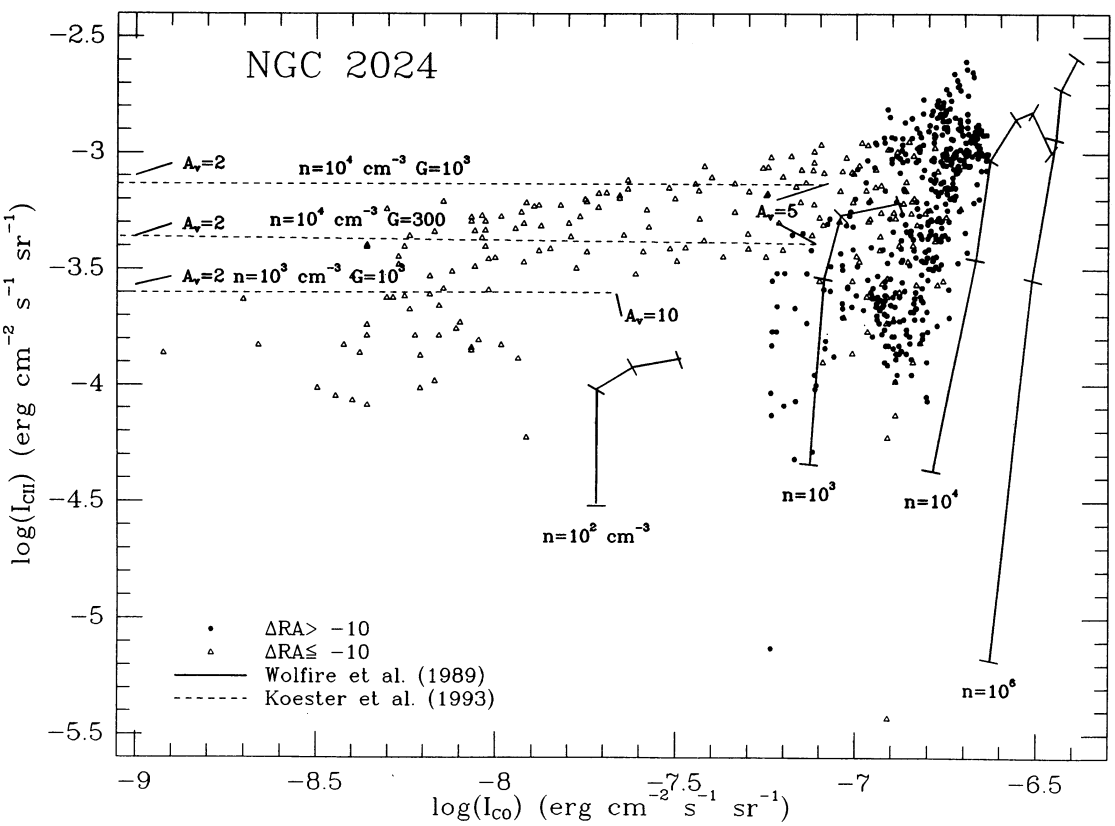

FIG. 4.—Relationship between [C II] and ^{12}CO $J = 1 \rightarrow 0$ intensities for the region north of $-02°03'$. Points less than 10′ west of the radio peak are shown as solid dots. Points $\geq$10′ west of the peak are shown as triangles. The solid lines show the semi-infinite plane parallel PDR models of Wolfire et al. (1989). The ticks along each constant density line began at $G_0 = 10$ and increase by factors of 10 for each tick (for $n = 10^6$ cm^{-3}, the models begin with $G_0 = 100$). The dashed lines show the finite thickness plane parallel models of Köster et al. (1994) for thicknesses corresponding to $A_V = 2$ to $A_V = 5$.

interior lie between the groups of models calculated for $n = 10^3$ and $n = 10^4$ cm^{-3} within a range in G_0 from ~ 30 to 10^4. The locus of these points in the part of the n, G_0 grid appropriate to the conditions present in NGC 2024 is a further indication that the plane-parallel PDR models account fairly well for the observed [C II] intensities. The steepness of the best-fit I([C II])–I(CO) relation indicates variations in the strength of the UV field are more significant than variations in density. The points from the inner few arcmin of NGC 2024 are somewhat brighter in [C II] than any of the models but this may be a geometry effect since the models are calculated for a single plane-parallel layer.

Since many of the points with high [C II]/CO $J = 1 \rightarrow 0$ intensity ratios lie well to the east of the macroscopic cloud boundary, having resolved the PDR at the cloud edge cannot always account for the high ratios. Another possible explanation for the high observed value of [C II]/CO is a gradual "thickening" of the cloud from west to east. In its simplest form, the cloud geometry would be wedgelike, with the molecular part of the wedge opening to the east. Given the apparent clumpiness of the gas, however, a more likely scenario is one in which the mean column density of clumps increases to the east. In this context, it is interesting to look at [C II] and CO $J = 1 \rightarrow 0$ intensities predicted by models which do not invoke semi-infinite clouds. The dashed lines in Figure 4 are based on the finite slab models of Köster et al. (1994). In these models, a plane of finite thickness is illuminated from both sides with UV radiation. The dashed lines in Figure 4 show how the I(CO)/I([C II]) relationship varies within families of models with a given UV field and density as the thickness of the slab is varied. One sees that models with reasonable values of n and G_0 and thicknesses corresponding to $A_V = 2$–5 can account for the measured strengths of the two lines in the western edge zone. In addition, a comparison of the Köster et al. models with the shallow slope of the I([C II])–I(CO) relation for the western cloud edge shows that variations in column density are the main cause for the distribution of the points.

4.2.2. *Dense Atomic and Molecular Components and the Structure of the Extended Cloud*

We have calculated beam-averaged C^+ column densities from the [C II] maps assuming that the opacity of the [C II] line is small. We have further assumed that the partition function correction, $N_{C^+}/N_{^2P_{3/2}} = 2$, which is a good approximation for $T = 100$–200 K and $n \gg 10^3$ cm^{-3}. These assumptions effectively make our C^+ column density a lower limit. Over broad regions around NGC 2024, the [C II] intensity is $\sim 1 \times 10^{-3}$ ergs cm^{-2} s^{-1} sr^{-1}, implying a beam-averaged C^+ column density of 8×10^{17} cm^{-2}. This column density is comparable to that predicted by plane-parallel PDR models (van Dishoeck & Black 1988).

We can use the ^{13}CO $J = 1 \rightarrow 0$ emission (Peterson & Bally 1994) to calculate similar beam-averaged column densities for the molecular material. Over much of the same part of the NGC 2024 region, the typical ^{13}CO intensity is 20–25 K km s^{-1}. This intensity implies $N(^{13}\mathrm{CO}) = 3 \times 10^{16}$ cm^{-2} and therefore a ratio of $N(C^+)/N(^{13}\mathrm{CO}) \sim 30$. Along the cross scan in the middle panel of Figure 2, a similar analysis of our ^{13}CO $J = 2 \rightarrow 1$ data yield $N(C^+)/N(^{13}\mathrm{CO}) = 40$–$80$. In deriving the ^{13}CO column densities, we have assumed that the lines are optically thin (measurements of $C^{18}O$ indicate that this is a reasonable assumption away from the molecular ridge) and that the level populations are in LTE with $T_K = 20$ K. The assumption that the level populations are in LTE will cause us to overestimate the total ^{13}CO column densities. The ^{13}CO $J = 1 \rightarrow 0$ intensities imply average H_2 column densities of 1–3×10^{22} cm^{-2}.

Over the bulk of the cloud, therefore, the C^+ and ^{13}CO column densities imply that the column densities of gas-phase carbon in the partially ionized atomic region and in the molecular region are comparable. If we determine the amount of CO bearing gas from ^{12}CO measurements using the canonical $I(^{12}\mathrm{CO})/N(H_2)$ ratio [$N(H_2)$ ratio [$N(H_2) = 3 \times 10^{20}$ I_{CO} cm^{-2}, where I_{CO} is given here in units of K km s^{-1}; Bloemen 1989], we get a similar result. One region which may have a dramatically lower $C^+/^{13}$CO column density ratio, however, is the narrow molecular ridge immediately behind the NGC 2024 H II region which is very opaque in the ^{13}CO lines (see Graf et al. 1993).

Counting all of the mapped region north of $-02°03'$, we derive a molecular cloud mass of 2100 $M_\odot$ from ^{13}CO, assuming $N(^{13}\mathrm{CO})/N(H_2) = 2 \times 10^{-6}$. Over the same region, the mass of the gas in the partially ionized (C^+) region is 180 $M_\odot$ for $N(C^+)/N(H + 2H_2) = 3 \times 10^{-4}$ and is 450 $M_\odot$ if the carbon in this region is depleted by the factor of 2.5 used in the van Dishoeck & Black (1988) PDR models. The mass of gas in the [C II] region may be an underestimate since we have determined the C^+ column densities conservatively (see also Stacey et al. 1991). It is therefore likely that the extended ($\sim 1.5 \times 2.5$ pc) region around NGC 2024 has greater than 10%–20% as much partially ionized atomic gas as dense molecular gas.

4.3. *Accounting for the Galactic* [C II] *Emission*

OB stars are born in molecular cloud cores. The destructive power of their UV radiation eventually frees the stars from the cores, allowing them to illuminate more extensive areas of the cloud surfaces. In extended sources in our own Galaxy and in external galaxies, the strength of the [C II] line alone does not give much information about the relationship between the dense gas and the OB stars. We want to use our L1630 data to help us interpret less detailed studies of more distant regions, in particular, to verify the usefulness of a simple indicator of the types of stars producing the UV flux and their distance from the PDRs they excite. The discussion in § 4.1.1 shows that most of the emission from NGC 2024 comes from an ionization front on the face of a cloud with an H II region on the outside. This geometry is common to many extended [C II] sources (e.g., M17; Matsuhara et al. 1989). We show here how emission from the H II region (in the form of radio continuum here, but also in Brγ or Brα) and the PDR (in the form of [C II] emission), can tell us about the spectral type of the illuminating stars and about their distance from the neutral material.

Figure 5 shows the dependence of the ratio of [C II] intensity to the 5 GHz flux density on main-sequence spectral type and distance. Appendix A explains how the line ratio is derived. Table 1 lists values for [C II] intensity, the 5 GHz flux density, and the ratio of the [C II] line intensity to the 5 GHz continuum specific intensity gathered from the literature for a small sample of galactic PDRs as well as for the galaxy M82. The table also gives the spectral type of the exciting stars derived from the radio continuum flux (except in Orion A, NGC 2023, and M16 where the stars have been typed from the optical spectra) and the scale size of the [C II] emission region. For resolved sources, one can, in principle, use the [C II] and [C II]/5 GHz data in Table 1 and the contours in Figure 5 to derive both the spectral type of the exciting star and the dis-

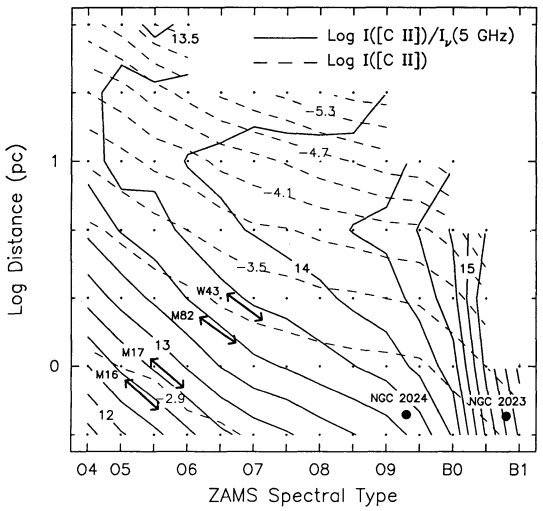

FIG. 5.—Ratio of [C II] 158 μm intensity to 5 GHz specific intensity (in Hz) arising at an ionization front as a function of the spectral type of the exciting star and of the distance between the star and the cloud (*solid lines*) as explained in § 4.3 and Appendix A. The dashed lines show log (I([C II])) in units of ergs cm^{-2} s^{-1} sr^{-1}, assuming a beam-filling factor of unity. The arrows indicate measured values for the ratio, taken from the literature and compiled in Table 1. The dots representing NGC 2923 and NGC 2024 lie at the intersection of the intensity ratio and the [C II] intensity listed for those sources.

tance of the star from the PDR/ionization front. In practice, this can only work well in regions where the [C II] and intensity ratio contours are fairly orthogonal and where the [C II] intensity is varying reasonably rapidly with spectral type or distance. These criteria are met for both sources from the current study listed in Table 1. We have plotted as arrows in Figure 5 the locus of the [C II]/5 GHz intensity ratios for the sources in Table 1. For NGC 2023 and NGC 2024, we use the measured [C II] intensity to localize the sources in the parameter space. The intersection of the [C II] intensity and intensity ratio contours for NGC 2024 lies at around O9.5 and 0.6 pc. These values compare well with the spectral type inferred from the radio continuum (also O9.5) and the scale size of the [C II] source (0.8 pc, which reflects the typical distance from the exciting star to the PDR). For NGC 2023, the intersection of the contours yields a spectral type of B1 and a size of $\sim$0.6 pc, as compared to the measured B1.5 and 0.3 pc. Figure 5 therefore seems like a reasonable tool for narrowing the possible range where a source can lie within the spectral type–distance to exciting star plane.

If we accept the validity of the assumptions which went into the derivation of the I([C II])/I_ν(5 GHz) relation (see Appendix), what can we learn from Figure 5 about more distant, less well-studied sources? In general, we can use only the intensity ratio and not the [C II] intensity since the area filling factor of the emission is unknown. Based on the data in Table 1, we see that the H II regions M17 and M16 lie in the lower left part of Figure 5. This is the region where the stars are very hot, O6–O7 or earlier, and the physical separation of the stars and the ionization fronts is small. Given the total UV flux inferrable from the radio continuum (in the case of M17) or the type of the hottest stars (M16), the actual location of these sources in Figure 5 is at the upper left end of the intensity ratio line where the stars are O4 or multiples of O4 and the size scales are around 1–3 pc. The [C II]/radio continuum intensity ratio from the inner 12′ (24 pc) of the giant H II region complex W43 lies between the ratio seen in M17 and that seen in M16. W43 must therefore also contain early O stars which lie within several parsecs of the [C II]–producing PDRs (see Thatte 1993). At 12′–18′ from the W43 complex, the [C II]/5 GHz ratio is comparable to that in NGC 2024. A broad, even distribution of late O and early B stars could produce the observed ratio but, given the large size scale involved, it is more likely that radiation from the central W43 cluster illuminates the extended PDR.

The ratio of [C II] intensity to the best estimate of the thermal portion of the 5 GHz flux density from the inner 60″ of M82 places the galaxy in the region in Figure 5 between NGC 2024 and M17. If the top of the main sequence in M82 lies near O8 (Rieke 1988), the typical separation of molecular cloud interfaces and the youngest O stars is $\sim$1 pc. This implies that the huge number of young stars in the central kiloparsec of M82 lie close to the remaining dense interstellar medium. The example of M82 illustrates how, if dense PDRs dominate the [C II] emission, Figure 5 can serve as a useful tool for studies of the state of the gas in starbursts. A low [C II]/radio continuum ratio implies that the young stars are closely connected to the dense gas (an ongoing starburst). A high ratio implies that

TABLE 1

[C II] AND RADIO CONTINUUM EMISSION

Source	log ($\langle I$[C II]$\rangle$) (ergs cm^{-2} s^{-1} sr^{-1})	Reference	S_ν(5 GHz) (ergs cm^{-2} s^{-1} Hz^{-1})	Reference	$\log\left(\frac{I([\text{C II}])}{I_\nu(5\text{ GHz})}\right)$ Hz	Spectral Type	Scale Size (pc)
Orion A	−2.5	1	4×10^{-21}	2	12.3	O5	0.4
NGC 2023	−3.3	3	3×10^{-25}	4	15.6	B1.5	0.3
NGC 2024	−3.0	3	6.5×10^{-22}	5	13.65	O9.5	0.8
M82	> −2.8	6	5×10^{-24}	7	13.45	...	...
M17	−2.9	8	5.4×10^{-21}	9	12.8	3 O4	5
M16 (inner 12′)	−3.4	10	1.7×10^{-21}	11	12.5	O4	3
W43 (inner 12′)	−3.1	12	8.0×10^{-22}	13	13.0	>3 O4	10
W43 (18′–30′)	−3.4	12	5×10^{-24}	14	13.7	...	40

REFERENCES.—(1) Stacey et al. 1993, averaged over a 4′ × 7′ area; (2) Wilson & Pauls 1984; (3) this work; (4) Pankonin & Walmsley 1976; (5) van der Werf et al. 1993; (6) Stacey et al. 1991; (7) Carlstrom & Kronberg 1991; (8) Matsuhara et al. 1989; (9) Wilson et al. 1979; (10) Nakagawa 1992; (11) Higgs et al. 1979, integrated over 12′; (12) Shibai et al. 1991; (13) Altenhoff et al. 1978, integrated over 12′; (14) Altenhoff et al. 1978, average flux density per 2′.6 beam along the [C II] cut of Shibai et al., background ($\sim$30%) subtracted.

the molecular gas has been expelled from the regions where the stars have formed. One might expect such a ratio in the later stages of starbursts.

We thank H. Störzer for providing the relevant quantities from the Köster et al. models, and R. Genzel and A. Sternberg for useful discussions. We thank N. Geis, U. Graf, J. Mangum, T. Phillips, and C. E. Walker for help with the observations and K. Peterson and J. Bally for making their data available in advance of publication. The airborne observations were supported in part by NASA grant NAG 2-402 to the University of Texas. The ground-based observations were supported by NSF grant AST-9017710 and the David and Lucile Packard Foundation. D. T. J. acknowledges the hospitality and support of the Max-Planck Institute für extraterrestrische Physik and the Alexander von Humboldt Stiftung.

APPENDIX A

THE [C II]–RADIO CONTINUUM RELATIONSHIP

Figure 6 illustrates the geometry upon which our calculation of the ratio of [C II] and 5 GHz radio continuum intensity (plotted as solid contours in Fig. 5) is based. A main-sequence OB star emitting N_L, Lyman continuum photons s^{-1} and having a total 6–13.6 eV luminosity L_{UV}, illuminates the surface of a molecular cloud distance X away. The Lyman continuum photons are absorbed at or near the cloud surface. The part of the cloud we are studying has radius r_c. As seen from the illuminating star, it has solid angle Ω_{SC}. A telescope at distance D observes the same cloud. The solid angle of the same part of the cloud as seen by the telescope is Ω_{TC}. If the resulting H II region is optically thin at 5 GHz and has an electron temperature of 10^4 K, we can write the observed flux density in the radio continuum as

$$S_\nu(5\ \mathrm{GHz}) = CN_L \frac{\Omega_{SC}}{4\pi D^2}\ \mathrm{ergs\ cm^{-2}\ s^{-1}\ Hz^{-1}}\ , \tag{A1}$$

where $C = 1.13 \times 10^{-64}$ (Rubin 1968).

The [C II] flux from the same cloud surface depends on the UV radiation field and on the density. We assume that the density is $n_{H2} \sim 10^4$ cm^{-3} and use the models of Hollenbach et al. (1991) and Wolfire, Tielens, & Hollenbach (1990) to determine the relationship between emergent [C II] intensity and incident far-UV intensity, $I([\mathrm{C\ II}]) = f(L_{UV}/X^2)$. The assumed density is reasonable for many H II region/molecular cloud interfaces and is high enough that the [C II] flux is relatively independent of density. The

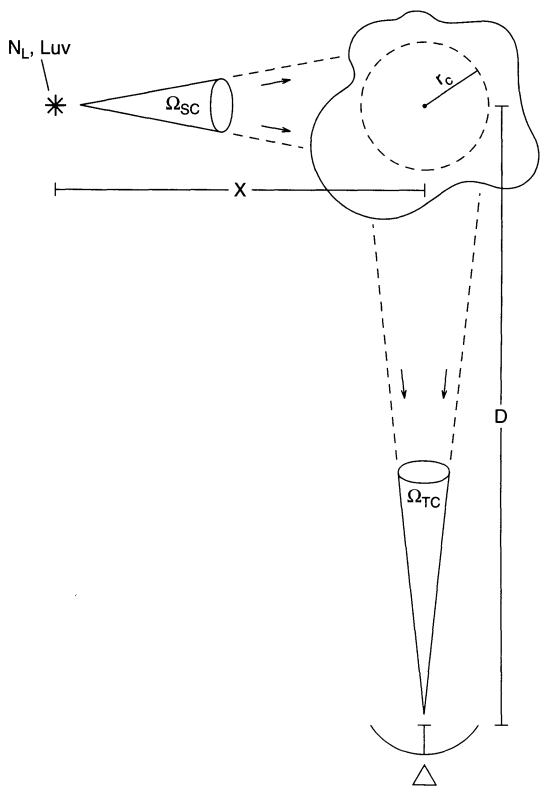

FIG. 6.—Schematic of the geometry assumed for the calculations used to create Fig. 5

observed [C II] flux is then

$$F([\mathrm{C\ II}]) = f\left(\frac{L_{\mathrm{UV}}}{X^2}\right)\Omega_{\mathrm{TC}}\ \mathrm{ergs\ cm^{-2}\ s^{-1}}\ . \tag{A2}$$

If we observe the same part of the cloud in both the radio continuum and in the [C II] line, we can divide the two equations, and the resulting ratio is equivalent to the ratio of [C II] intensity to specific intensity in the radio continuum over that part of the cloud:

$$\frac{I([\mathrm{C\ II}])}{I_\nu(5\ \mathrm{GHz})} = \frac{4\pi D^2 f(L_{\mathrm{UV}}/X^2)\Omega_{\mathrm{TC}}}{CN_{\mathrm{Ly}}\Omega_{\mathrm{SC}}}\ \mathrm{Hz}\ . \tag{A3}$$

We can rewrite the solid angles in this equation as

$$\Omega_{\mathrm{SC}} = \frac{\pi r_c^2}{X^2}\ , \tag{A4}$$

and

$$\Omega_{\mathrm{TC}} = \frac{\pi r_c^2}{D^2}\ , \tag{A5}$$

yielding the relation

$$\frac{I([\mathrm{C\ II}])}{I_\nu(5\ \mathrm{GHz})} = \frac{4\pi X^2 f(L_{\mathrm{UV}}/X^2)}{CN_{\mathrm{L}}}\ . \tag{A6}$$

The intensity ratio depends on the number of Lyman continuum photons s^{-1} emitted by the star and on the stellar UV luminosity—both functions of the spectral type, as well as on the distance between the star and the cloud. Using the radio continuum or Brackett line flux rather than far-IR luminosity in the ratio makes it sensitive to stellar surface temperature rather than simply to the incident far-UV flux. Figure 5 shows the ratio of the [C II] intensity to the 5 GHz flux density in the space of main-sequence spectral type versus distance derived under these assumptions. The value of $I([\mathrm{C\ II}])/I_\nu(5\ \mathrm{GHz})$ increases initially along both axes as the radio continuum intensity drops linearly with decreasing N_{L} while the [C II] intensity depends only logarithmically on L_{UV}. At the extreme right, the ratio increases very rapidly as the stellar surface temperatures drop to the point where the Lyman continuum is on the Wien side of the stellar energy distribution and N_{L} drops much more rapidly than L_{UV}. The double-valued nature of the ratio as a function of distance at constant spectral type results from the sudden decrease in the [C II] intensity at the point where the UV field is insufficient to heat the gas enough to populate the $C^+\ ^2P_{3/2}$ state. In the case of nearby sources where we can assume an area filling factor of unity, we can also plot the [C II] intensity in the same space (*dashed lines*).

There are a number of possible pitfalls introduced by the assumptions in the derivation of the $I([\mathrm{C\ II}])/I_\nu(5\ \mathrm{GHz})$ relation. Our implicit assumption that the PDR projects the same fraction of its surface as seen from the exciting star and the observer leads to errors in placing sources in the diagram. The models assume that the regions are plane-parallel which probably results in a systematic underestimate of the [C II] intensity at a given UV field strength. For sources with particularly high incident far-UV fields (Orion A, for example), the [C II] intensity is insensitive to the strength of the field and geometric effects can alter this intensity significantly. The [C II] to radio continuum intensity ratio for Orion A lies within the parameter space shown in Figure 5, but the [C II] intensity does not (Table 1). For larger scale sources or sources with less intense UV fields, Figure 5 has more predictive value. The [C II] line to 5 GHz continuum ratio varies by a factor of ~ 2000 in the sources listed in Table 1. This range is far larger than the dispersion caused by uncertainties in source geometry. Other uncertainties arise from our physical assumptions. In constructing Figure 5, we have assumed that all of the gas is dense which may result in an overestimate of $I([\mathrm{C\ II}])$ for a given UV field. In the inner Galaxy and in other galaxies, the radio continuum may be largely nonthermal. Estimates of the denominator for Figure 5 based on Brγ or Brα measurements would circumvent this problem. The assumption that all the [C II] emission arises in the PDR may not always be valid. There are good arguments for a contribution to the [C II] by extended low-density H II regions, especially on large scales in the inner galaxy. What the locations in Figure 5 of sources from Table 1 imply is that it is in principle possible to explain the observed properties of inner galaxy regions with PDR material alone. The argument does not rule out the ELD H II contribution, however. The effects of these problems need to be investigated as we assess the usefulness of the [C II]/radio continuum ratio as a diagnostic in the light of future observations.

REFERENCES

Altenhoff, W. J., Downes, D., Pauls, T., & Schraml, J. 1978, A&AS, 35, 23
Anthony-Twarog, B. J. 1982, AJ, 87, 1213
Barnes, P. J., Crutcher, R. M., Bieging, J. H., Storey, J. W. V., & Willner, S. P. 1989, ApJ, 342, 883
Bash, F. N., Green, E., & Peters, W. L. 1977, ApJ, 217, 464
Bloemen, H. 1989, ARA&A, 27, 469
Carlstrom, J. E., & Kronberg, P. P. 1991, ApJ, 366, 422
Crawford, M. K., Genzel, R., Townes, C. H., & Watson, D. M. 1985, ApJ, 291, 755
Crutcher, R. M., Henkel, C., Wilson, T. L., Johnston, K. J., & Bieging, J. H. 1986, ApJ, 307, 302
de Jong, T., Dalgarno, A., & Boland, W. 1980, A&A, 91, 68
Graf, U. U., Eckart, A., Genzel, R., Harris, A. I., Poglitsch, A., Russell, A. P. G., & Stutzki, J. 1993, ApJ, 405, 249
Higgs, L. A., Doherty, L. H., MacLeod, J. M., & Terzian, Y. 1979, AJ, 84, 77
Hollenbach, D. J., Takahashi, T., & Tielens, A. G. G. M. 1991, ApJ, 377, 192
Howe, J. E., Jaffe, D. T., Genzel, R., & Stacey, G. J. 1991, ApJ, 373, 158
Jaffe, D. T., Genzel, R., Harris, A. I., Howe, J. E., Stacey, G. J., & Stutzki, J. 1990, ApJ, 353, 193
Köster, B., Störzer, H., Stutzki, J., & Sternberg, A. 1994, A&A, 284, 545
Krügel, E., Thum, C., Martin-Pintado, J., & Pankonin, V. 1982, A&AS, 48, 345
Kurtz, N. T., Smyers, S. D., Russell, R. W., Harwit, M., & Melnick, G. 1983, ApJ, 264, 538
Kurucz, R. L. 1979, ApJS, 40, 1
Lada, E. A. 1990, Ph.D. thesis, Univ. Texas at Austin
Lada, E. A., Bally, J., & Stark, A. A. 1991, ApJ, 368, 432
Madden, S. C., Geis, N., Genzel, R., Herrmann, F., Jackson, J. M., Poglitsch, A., Stacey, G. J., & Townes, C. H. 1993, ApJ, 407, 579
Matsuhara, H., et al. 1989, ApJ, 339, L67
Mezger, P. G. 1978, A&A, 70, 565

Mezger, P. G., Chini, R., Kreysa, E., Wink, J. E., & Salter, C. J. 1988, A&A, 191, 44
Moore, T. J. T., Chandler, C. J., Gear, W. K., & Mountain, C. M. 1989, MNRAS, 237, 1P
Nakagawa, T. 1993, in ASP Conf. Proc. 41, Astronomical Spectroscopy: Future Observational Directions, ed. S. Kwok, 373
Nakagawa, T., et al. 1993, in Back to the Galaxy, ed. S. S. Holt & F. Verter, in AIP Conf. Proc. 278, 303
Panagia, N. 1973, AJ, 78, 929
Pankonin, V. L., & Walmsley, C. M. 1976, A&A, 48, 341
Peterson, K., & Bally, J. 1994, ApJ, to be submitted
Poglitsch, A., et al. 1991, Int. J. Infrared Millimeter Waves, 12, 859
Rieke, G. H. 1988, in Galactic and Extragalactic Star Formation, ed. R. E. Pudritz & M. Fich (Dordrecht: Kluwer), 561
Rubin, R. H. 1968, ApJ, 154, 391
Schulz, A., Güsten, R., Zylka, R., & Serabyn, E. 1991, A&A, 246, 570
Shibai, H., et al. 1991, ApJ, 374, 522
Stacey, G. J., Beeman, J. W., Haller, E. E., Geis, N., Poglitsch, A., & Rumitz, M. 1992, Int. J. Infrared Millimeter Waves, 13, 1689
Stacey, G. J., Geis, N., Genzel, R., Lugten, J. B., Poglitsch, A., Sternberg, A., & Townes, C. H. 1991, ApJ, 373, 423
Stacey, G. J., Jaffe, D. T., Geis, N., Genzel, R., Harris, A. I., Poglitsch, A., Stutzki, J., & Townes, C. H. 1993, ApJ, 404, 219
Stacey, G. J., Viscuso, P. J., Fuller, C. E., & Kurtz, N. T. 1985, ApJ, 289, 803
Sternberg, A., & Dalgarno, A. 1989, ApJ, 338, 197
Stutzki, J., Stacey, G. J., Genzel, R., Harris, A. I., Jaffe, D. T., & Lugten, J. B. 1988, ApJ, 332, 379
Thatte, N. 1993, Ph.D. thesis, Univ. California, Berkeley
Thronson, H. A., Lada, C. J., Schwartz, P. R., Smith, H. A., Smith, J., Glaccum, W., Harper, D. A., & Loewenstein, R. F. 1984, ApJ, 280, 154
Tielens, A. G. G. M., & Hollenbach, D. J. 1985, ApJ, 291, 722
van der Werf, P. P., Goss, W. M., Heiles, C., Crutcher, R. M., & Troland, T. H. 1993, ApJ, 411, 247
van Dishoeck, E. F., & Black, J. H. 1988, ApJ, 334, 771
Wilson, T. L., Fazio, G. G., Jaffe, D., Kleinmann, D., Wright, E. L., & Low, F. J. 1979, A&A, 76, 86
Wilson, T. L., & Pauls, T. 1984, A&A, 138, 225
Wolfire, M. G., Hollenbach, D., & Tielens, A. G. G. M. 1989, ApJ, 344, 770
Wolfire, M. G., Tielens, A. G. G. M., & Hollenbach, D. 1990, ApJ, 358, 116
Wright, E. L., et al. 1991, ApJ, 381, 200
Zhou, S., Jaffe, D. T., Howe, J. E., Geis, N., Herrmann, F., Madden, S. C., Poglitsch, A., & Stacey, G. J. 1993, ApJ, 419, 190